IEEE Access
Multidisciplinary | Rapid Review | Open Access Journal

Received June 3, 2018, accepted July 2, 2018, date of publication July 23, 2018, date of current version August 20, 2018.

Digital Object Identifier 10.1109/ACCESS.2018.2859021

A Simplified Subdomain Analytical Model for the Design and Analysis of a Tubular Linear Permanent Magnet Oscillation Generator

RONG GUO, HAITAO YU, TAO XIA, ZHENCHUAN SHI, WEIBO ZHONG, AND XIAOMEI LIU
School of the Electrical engineering, Southeast University, Nanjing 210096, China

Corresponding author: Haitao Yu (htyu@seu.edu.cn)

This work was supported in part by the Natural Science Foundation of China under Grant 41576096 and in part by the Fundamental Research Funds for the Central Universities and Postgraduate Research and Practice Innovation Program of Jiangsu Province under Grant KYCX17_0083.

ABSTRACT We present a simplified 2-D analytical subdomain model to predict the open-circuit magnetic field of a tubular linear permanent magnet oscillation generator (T-LPMOG) to account for its primary and secondary end effects. At present, the magnetic field calculations of the T-LPMOG are typically analyzed in cylindrical coordinates, and the end effect is neglected accordingly to apply the periodic boundary. In this paper, a simplified 2-D analytical subdomain model in polar coordinates is proposed to consider the end effect. First, a coordinate transformation method is adopted to establish the 2-D subdomain analytical model, the cylindrical coordinates are converted into polar coordinates, and the T-LPMOG is analyzed under this new coordinate system. Next, the subdomain method is used to analyze the analytical model by solving Laplace's equation and the Poisson equation. Based on the simplified analytical model, the flux density and back-electromotive force are obtained. The analytical results are verified using the finite element analysis (FEA) method, and the computational times compared with the FEA method are provided. Finally, a T-LPMOG prototype is manufactured and tested, and the results show that the proposed analytical model can be useful in the initial design and optimization of the T-LPMOG.

INDEX TERMS Coordinate transformation method, subdomain model, magnetic field, end effect, slot effect, T-LPMOG.

I. INTRODUCTION

The increasing demand for energy has focused new attention on renewable resources. In the case of reciprocating linear vibration, such as wave power generation, nuclear power generation, and aeronautics, the tubular linear permanent magnet oscillation generator (T-LPMOG) is a viable option [1]–[3]. The T-LPMOG can provide direct linear drive without any intermediate transmission links; thus, this component has the outstanding advantages of high efficiency, a high power factor, fast response, energy-saving capability, and maintenance-free operation, among other advantages [4]–[6]. However, unlike rotary motors, the thrust ripple of the T-LPMOG is caused primarily by the end effect force; this characteristic is a substantial drawback that introduces acoustic noise, mechanical vibration, and a severely distorted magnetic field [7]–[9]. Accurate prediction of the magnetic field distribution is important because such accuracy directly affects the electromagnetic performance of the machine.

Recently, several numerical and analytical methods have been employed to solve the magnetic field problem of the T-LPMOG. In [10]–[13], the finite element method (FEM) was adopted to analyse the magnetic field and calculate the associated electromechanical parameters. This method offers high accuracy and incorporates the influence of nonlinear factors. However, FEM analysis remains relatively slow and time consuming. In [14]–[18], a magnetic equivalent circuit (MEC) was used to analyse the electromagnetic field inside the motor because the MEC can account for the nonlinearity, armature reaction, and end effect, among other parameters. Nevertheless, this method calculates the magnetic field only at several discrete points of the structure, and it lacks adequate precision. The analytical model based on the subdomain method is increasingly used in the design of various permanent magnet motors because this method can provide more accurate predictions of the magnetic field distribution. In [19]–[21], the slotless analytical model was used to predict the air-gap field distribution of permanent magnet machines with internal and external rotors. The armature reaction field produced by the stator windings was also considered. In [22], a tubular slotless linear motor with surface-mounted permanent magnets (SMPMs) was analysed, the magnetic field strength and flux density were calculated based on Maxwell's equations, and the analytical results were verified using finite element analysis (FEA) methods. In [23] and [24], the magnetic field of the air gap was derived using a semi-analytical framework, the Schwarz-Christoffel (SC) conformal mapping method was adopted to consider the slotting effects, and the tubular actuator was modelled as a linear actuator by taking into account the axial symmetry of the permanent-magnet tubular linear actuator. In [25], an improved conformal mapping (ICM) method was proposed to model the magnetic induction inside a permanent magnet; the armature reaction, slotting effect, magnetic saturation, and relative recoil permeability were considered. The ICM method is useful for on-load performance analysis of SMPM motors. In [26]–[28], a 2-D relative permanence function was introduced to consider the slotting effect, and the air-gap flux density was obtained by multiplying the slotless air-gap flux density by this relative permanence function. In [29]–[31], the magnetic field distribution in the slotted air gap of the SMPM and Halbach PM motors was calculated using a complex relative permeance function, providing both the radial and tangential components of the flux density. In [32] and [33], an analytical model was presented to calculate the flux density distribution in PM motors, the effects between the pole transitions and slot openings were considered, and the instantaneous field distribution in the slot regions where the magnet pole transition passes over the slot opening was calculated. The magnetic field and forces can be calculated highly accurately with this analytical model. In [34], an exact 2-D analytical model in polar coordinates was presented to predict the magnetic field in PM machines. Different magnetizations, including radial and parallel magnetization, were considered, and the slot effect was the main innovation in this model. The open-circuit magnetic field distribution was derived using this analytical model, and the amplitude and waveform of the analytical results match well with those of FEA. In [35] and [36], an exact 2-D subdomain model was developed to analyse the magnetic field distribution in SMPM machines. The slot effect was considered, and the magnetic field distributions of no-load and armature reaction were calculated based on this model. In [37], a double-sided LTPMS machine with NN magnetization and NS magnetization were analysed based on the analytical method. The flux density distributions in the air gap and on the stator surface were calculated using the vector potential. In [38], an analytical method was used to analyse a tubular-linear permanent magnet synchronous machine (T-LPMSM), and Bessel functions were adopted to predict the air-gap flux density. In addition, three structures, i.e., the infinite length machine, a finite length machine and a finite length machine with quasi-cancellation of the end effect, were discussed. The phase flux linkages and back-electromotive force (back-EMF) were calculated based on this method. In [39], an improved analytical subdomain model was proposed to predict the magnetic field of LPMSMs, and the semi-closed slot effect and end effect were considered. The variable separation method and boundary conditions were applied to solve the magnetic field in each subdomain, and the forces were calculated based on the Maxwell stress theory. In [40], an analytical model was established in 2-D polar coordinates to analyse the SMPM machine with a parallel magnetized magnet. A detailed analytical solution was presented, and the governing equations of the magnetic field were derived based on this analytical model. The analytical model has high accuracy and efficiency for predicting the air-gap magnetic field distribution. In [41]–[43], the subdomain method was used to resolve surface permanent magnet machines. Tooth tips, open circuits, armature reactions, and on-load field distributions were predicted. Among these factors, armature reactions with non-overlapping and overlapping windings were calculated. Flux density, cogging torque, back-EMF, electromagnetic torque, and winding inductances were obtained based on this subdomain model. Moreover, FEA was performed to validate the analytical model, and the results show that the analytical model has high accuracy for predicting electromagnetic performance.

When using the analytical models noted above, the magnetic fields are typically calculated based on the assumption that the secondary length of the linear machine is infinite for the application of periodic boundary conditions in the analysis. However, according to this assumption, the end effect is ignored. In the present study, a simplified 2-D analytical subdomain model is proposed to design and analyse the T-LPMOG, both the primary and secondary end effects are considered using the coordinate transformation method. First, a simplified 2-D analytical model is established in the polar coordinates instead of the cylindrical coordinates to reduce the number of calculation regions and the complexity of the solution. Next, the variable separation method is used to derive the analytical field expression of each subdomain by solving Laplace's equation and Poisson's equation; then, the coefficients in the magnetic field expression are determined by applying the boundary and interface conditions. The slot effect is considered using the conformal capping method. Based on the simplified analytical model, the flux density and back-EMF are calculated. Finally, the analytical results are verified through FEA and experiments. The results show that the proposed analytical model can accurately predict the performance of a linear configuration, verifying the utility of the model in the initial design and optimization processes of the T-LPMOG.

II. ANALYTICAL MODEL OF THE T-LPMOG

A 3-D finite-element model of the T-LPMOG in cylindrical coordinates is shown in Fig. 1(a), and according to the axial symmetry of the T-LPMOG, the corresponding quasi-2-D model is shown in Fig. 1(b). If the primary and secondary end effects are both considered, the magnetic field can be divided into 12 subdomain regions: infinite region 1, back-iron region 2, PM region 3, air-gap region 4, slot region 5, exterior region 6, primary end regions 5-1 and 5-2, and secondary end regions 2-1, 2-2, 3-1, and 3-2. These subdomain regions render the field calculations complex. To reduce the computational complexity, the simplified T-LPMOG analytical model in polar coordinates is used. The top subdomains of end regions 2-1, 3-1, and 5-1 are extended to the top boundary $x = +\propto$, and the bottom subdomains 2-2, 3-2, and 5-2 extend to the bottom boundary $x = -\propto$. According to the symmetry principle, the model can be bent into an arc structure with radius $r \rightarrow \propto$, and if the length of the secondary L_{ex} is finite, the radius of the simplified model in polar coordinates r will also be finite [1] [39]. By connecting the top and bottom boundaries, Fig. 1(c) can be obtained. In Fig. 1(c), primary end subdomains 5-1 and 5-2 are converted into subdomain 3, and the secondary end effect is mainly caused by the interaction between the PMs and the primary stator iron. Extension of the secondary back-iron has little influence on the magnetic field distribution, and thus, the secondary end subdomains 2-1, 2-2, 3-1, and 3-2 are combined in subdomain 1. The secondary end effect is considered because the PM is mounted on part of the surface of the back iron. From Fig. 1(c), the number of subdomain regions is reduced from 12 to 6, considering both end effects and slot effects. In polar coordinates, the entire domain of the magnetic field can be divided into five subdomains: 1) PM region; 2) air-gap region; 3) end region; 4) exterior air region; and 5) slot region.

In Fig. 1, θ_{mv} and θ_s represent the mover and stator coordinate systems, respectively. θ_1 represents the span angle stator, and θ_{vs} is the mechanical angular position between the mover and the stator. R_i and R_b are the inner and outer radii of secondary iron, respectively. R_{pm} is the outer radius of PM, and R_g is the outer radius of the gap. R_s is the outer radius of the stator. R_{sa} is the outer radius of the teeth. L_{ex} is the extended length of secondary iron.

To calculate the magnetic field distribution accurately, parameter conversion is important, and the dimensions of the model must remain unchanged. The equivalent formulas are determined as follows:

$$R_{pm} = L_{ex}/2\pi \tag{1}$$

$$\theta_1 = L_s/L_{ex} \times 2\pi \tag{2}$$

III. MAGNETIC FIELD EQUATION AND ANALYTICAL SOLUTION OF THE T-LPMOG

The simplified subdomain model in Fig. 1(c) is used to analyse the magnetic field of the T-LPMOG. Certain assumptions are made to facilitate the analytical solution [35]:

1) The permeability of the stator and back-iron are infinite;
2) The permeability of the permanent magnets is assumed to be equal to that of air;

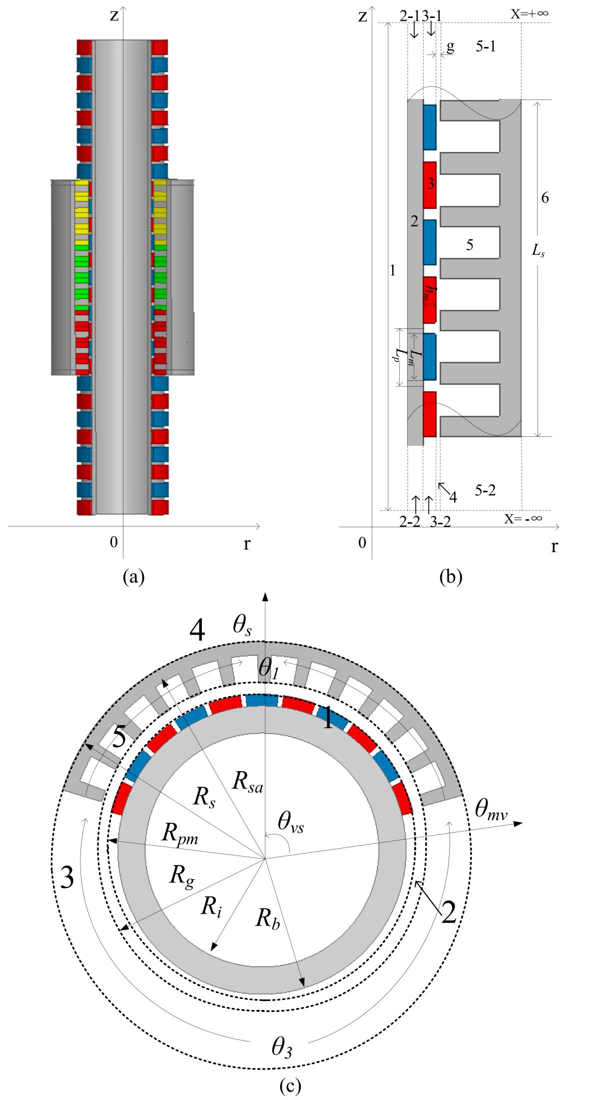

FIGURE 1. **FEA simulation model and analytical models of the T-LPMOG. a. FEA simulation model of the T-LPMOG. b. Corresponding quasi-2 D model of the T-LPMOG in cylindrical coordinates. c. Simplified 2 D model of the T-LPMOG in polar coordinates.**

3) The electrical conductivity and eddy current of the PMs are neglected.

A. MAGNETIZATION VECTOR DISTRIBUTION OF THE PMs

Radial magnetization is applied to the permanent magnet in this simplified model, and the distribution of the magnetization vector $\overrightarrow{M}$ varies with the position. In 2-D polar coordinates, the magnetization vector $\overrightarrow{M}$ is separated into two directions and can be expressed as follows:

$$\overrightarrow{M} = M_r \cdot \overrightarrow{r} + M_\theta \cdot \overrightarrow{\theta_{mv}} \tag{3}$$

where M_r and M_θ represent the radial and tangential magnetization vectors of $\overrightarrow{M}$, respectively, and θ_{mv} represents the mechanical angular position of the mover.

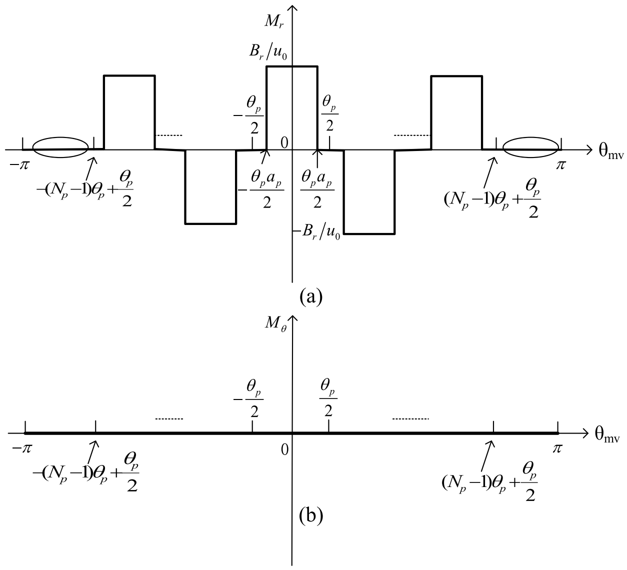

FIGURE 2. Distribution of the magnetization vector $\vec{M}$. a. Distribution of the radial components of the magnetization vector $\vec{M}$. b. Distribution of the tangential components of the magnetization vector $\vec{M}$.

For radial magnetization, the magnetization along the tangential direction is zero, and due to consideration of the primary and secondary end-effect problems, the magnetization distribution along the radial direction in the mover coordinate system is shown in Fig. 2. The values from $\pm[(N_p-1)\theta_p+\theta_p/2]$ to $\pm\pi$ are zero. In addition, when the PM moves with $\theta_{vs}=\omega t+\theta_{0s}$, where ω is the mover speed and θ_{0s} is the initial angle, according to the formula $\theta_s=\theta_{mv}+\theta_{vs}$, the radial magnetization formula in the stator coordinate can be derived.

According to the Fourier series method, the radial component and tangential component of the magnetization vector M can be obtained as follows:

$$\begin{cases} M_r(\theta_s)=\sum_{n=1}^{\infty}[M_{rcn}\cos(n\theta_s)+M_{rsn}\sin(n\theta_s)] \\ M_\theta(\theta_s)=\sum_{n=1}^{\infty}[M_{\theta cn}\cos(n\theta_s)+M_{\theta sn}\sin(n\theta_s)] \end{cases} \tag{4}$$

where

$$M_{rcn}=\frac{2B_r}{n\pi\mu_0}\sin(\frac{\theta_p\alpha_p}{2})+\sum_{i=2}^{Np}(-1)^{i-1}(\frac{4B_r}{n\pi\mu_0})\cos(\frac{(i-1)n\theta_p}{2})\sin(\frac{n\theta_p\alpha_p}{2}) \tag{5}$$

$$M_{rsn}=-\frac{2B_r}{n\pi u_0}(\cos(\frac{n\theta_p\alpha_p}{2})-1)+\sum_{i=2}^{Np}(-1)^{i-1}(\frac{4B_r}{n\pi\mu_0})\sin(\frac{(i-1)n\theta_p}{2})\sin(\frac{n\theta_p\alpha_p}{2}) \tag{6}$$

$$M_{\theta cn}=M_{\theta sn}=0 \tag{7}$$

where, a_p represents the pole pitch, and N_p is the number of PMs. B_r represents the remanence flux density of the PM, and μ_0 is the vacuum permeability.

B. VECTOR POTENTIAL AND GENERAL SOLUTION EQUATION OF THE MAGNETIC FIELD

To calculate the magnetic flux density B, the vector magnetic potential A is introduced to describe the general equation. The expressions for the radial and tangential magnetic flux densities are derived as follows:

$$B_r=\frac{1}{r}\frac{\partial A_z}{\partial\theta}\quad\text{and } B_\theta=-\frac{\partial A_z}{\partial r} \tag{8}$$

where, A_z represents the axial component of the magnetic vector potential.

The partial differential equation of the magnetic field can be expressed based on the vector potential. Poisson's equation and Laplace's equation in each region are defined as follows:

$$\frac{\partial^2A_{z1}}{\partial r^2}+\frac{1}{r}\frac{\partial A_{z1}}{\partial r}+\frac{1}{r^2}\frac{\partial^2A_{z1}}{\partial\theta_s^2}=-\frac{\mu_0}{r}(M_\theta-\frac{\partial M_r}{\partial\theta_s})\quad(i=1) \tag{9}$$

$$\frac{\partial^2A_{zi}}{\partial r^2}+\frac{1}{r}\frac{\partial A_{zi}}{\partial r}+\frac{1}{r^2}\frac{\partial^2A_{zi}}{\partial\theta_s^2}=0\quad(i=2\ldots6) \tag{10}$$

In 2-D polar coordinates, according to the separation of variables, the general solution equations for each subdomain region can be derived.

1) In the PM region (region 1)

The general solution of state (9) is written as follows:

$$A_{z1}=\sum_{n=1}^{\infty}[A_{1n}(r/R_{pm})^n+B_{1n}(r/R_b)^{-n}]\cos(n\theta_s)+\sum_{n=1}^{\infty}[C_{1n}(r/R_{pm})^n+D_{1n}(r/R_b)^{-n}]\sin(n\theta_s)+A_p \tag{11}$$

where A_{1n}, B_{1n}, C_{1n}, and D_{1n} are the integration coefficients that must be determined. n represents the nth harmonic. A_p is a particular solution that can be found as follows [38]:

$$A_p=\begin{cases} \mu_0r\sum_{n=1}^{\infty}\frac{Inr}{2}(M_{rsn}\cos(n\theta_s)-M_{rcn}\sin(n\theta_s)) \\ (n=1) \\ \mu_0r\sum_{n=1}^{\infty}\frac{1}{n^2-1}(-nM_{rsn}\cos(n\theta_s)+nM_{rcn}\sin(n\theta_s)) \\ (n\neq1) \end{cases} \tag{12}$$

On the back-iron surface, the core permeability is regarded as infinite; i.e., the magnetic flux lines are perpendicular to the surface of the core, and the tangential components of the magnetic flux density B and the magnetic field strength H are zero. The boundary condition is expressed as follows:

$$H_{1r}|_{r=R_b}=-\frac{1}{\mu_0\mu_r}\qquad B_{1r}|_{r=R_b}-\frac{1}{\mu_r}M_\theta=0 \tag{13}$$

According to equation (13), the coefficient can be determined as follows:

$$B_{1n} = \frac{\mu_0 R_b}{n}\left(\frac{M_{\theta cn} - nM_{rsn}}{n^2-1} + M_{\theta cn}\right) + A_{1n}E_{1n} \tag{14}$$

$$D_{1n} = \frac{\mu_0 R_b}{n}\left(\frac{M_{\theta sn} + nM_{rcn}}{n^2-1} + M_{\theta sn}\right) + C_{1n}E_{1n} \tag{15}$$

with

$$E_{1n} = (r/R_{pm})^n \tag{16}$$

The vector potential given by equation (11) can be rewritten as

$$A_{z1} = \sum_{n=1}^{\infty}(F_{1n(r)}A_{1n} + F_{2n(r)}M_{\theta cn} - F_{3n(r)}M_{rsn})\cos(n\theta_s) + \sum_{n=1}^{\infty}(F_{1n(r)}C_{1n} + F_{2n(r)}M_{\theta sn} + F_{3n(r)}M_{rcn})\sin(n\theta_s) \tag{17}$$

where

$$F_{1n(r)} = \left[\left(\frac{r}{R_{pm}}\right)^n + E_1\left(\frac{R_b}{r}\right)^n\right] \tag{18}$$

$$F_{2n(r)} = \begin{cases} \frac{\mu_0}{2}[R_b(1-InR_b)(\frac{R_b}{r}) - rInr] & (n=1) \\ \frac{\mu_0}{n^2-1}[r + R_b n(\frac{R_b}{r})^n] & (n \neq 1) \end{cases} \tag{19}$$

$$F_{3n(r)} = \begin{cases} -\frac{\mu_0}{2}[rInr + R_b(1+InR_b)(\frac{R_b}{r})] & (n=1) \\ \frac{\mu_0}{n^2-1}[nr + R_b(\frac{R_b}{r})^n] & (n \neq 1) \end{cases} \tag{20}$$

2) In the air-gap region (region 2)

The general solution equation for equation (8) in the air-gap region is expressed as follows:

$$A_{z2} = \sum_{n=1}^{\infty}[A_{2n}(r/R_g)^n + B_{2n}(r/R_{pm})^{-n}]\cos(n\theta_s) + \sum_{n=1}^{\infty}[C_{2n}(r/R_g)^n + D_{2n}(r/R_{pm})^{-n}]\sin(n\theta_s) \tag{21}$$

where A_{2n}, B_{2n}, C_{2n} and D_{2n} are integration coefficients to be determined.

3) In the end region (region 3)

To consider both the primary and secondary end effects, the structure of the machine in the end region is in the shape of an arc. Unlike in the air-gap region, the radian angle is θ_3 instead of 2π, and the equation must be transformed as follows:

$$A_{z3} = \sum_{k=1}^{\infty}[A_{3k}G_{31k} + B_{3k}G_{32k}]\cos\frac{k\pi}{\theta_3}\left(\theta_s + \frac{\theta_3}{2} - \pi\right) \tag{22}$$

with

$$G_{31k} = (r/R_s)^{k\pi/\theta_3} \quad G_{32k} = \left(r/R_g\right)^{-k\pi/\theta_3} \tag{23}$$

where, A_{3k} and B_{3k} are integration coefficients to be determined. k represents the kth harmonic in the end region.

4) In the exterior region (region 4)

Since regions 2 and 4 are distributed over 2π, the general expression solutions in these two regions are the same. When region 4 extends indefinitely in the circumferential direction, the vector potential is infinite; thus, the expression can be redefined as follows:

$$A_{z4} = \sum_{n=1}^{\infty}[B_{4n}G_{4n}\cos(n\theta_s) + D_{4n}G_{4n}\sin(n\theta_s)] \tag{24}$$

with

$$G_{4n} = (r/R_s)^{-n} \tag{25}$$

where B_{4n} and D_{4n} are the integration coefficients to be determined.

5) In the slot region (region 5)

The subdomain method can be used to calculate the magnetic field distribution in the stator slot accurately. However, with an increasing number of boundary conditions, the magnetic field equations must be incorporated, causing the solution process to become more complex; in addition, an explicit expression for the magnetic field is not available [28].

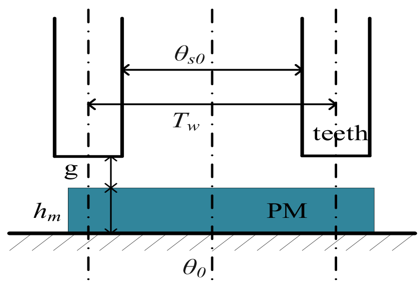

FIGURE 3. Single-slot modelling of the T-LPMOG.

In this study, a 2-D relative permeance function is adopted to analyse the effect of stator slotting; the single-slot model is shown in Fig. 3, and the functional equation is obtained as follows [26]:

$$\tilde{\lambda}(\theta_s, r) = \lambda(\theta_s, r)/\Lambda_0$$

$$\lambda(\theta_s, r) = \begin{cases} \Lambda_0\{1 - \beta(r) - \beta(r)\cos[5\pi/4\theta_{s0}(\theta_s - \theta_0)]\} \\ (\theta_s \in (\theta_0 - 0.8\theta_{s0} \leq \theta_s \leq \theta_0 + 0.8\theta_{s0})) \\ \Lambda_0, \quad else \end{cases} \tag{26}$$

where θ_{s0} represents the slot-opening angle and Λ_0 is the permeance, the expressions are as follows:

$$\begin{cases} \theta_{s0} = w_s\theta_1/L_s \\ \Lambda_0 = \mu_0/(g + h_m/u_r) \end{cases} \tag{27}$$

The function $\beta(r)$ can be derived using the conformal transformation method:

$$\beta(r) = 1/2[1 - 1/\sqrt{1 + (w_s/2g_1)^2(1+v^2)}] \tag{28}$$

where w_s represents the slot width, g_1 is the effective air gap, and v can be determined by

$$\begin{cases} y\pi/w_s = 1/2In[\sqrt{a^2+v^2} + v/\sqrt{a^2+v^2} - v] \\ \qquad + 2g_1/w_s \arctan(2g_1 v/w_s\sqrt{a^2+v^2}) \end{cases} \tag{29}$$

and

$$a^2 = 1 + (2g'/w_s)^2 \tag{30}$$
$$y = r - R_g + g_1 \tag{31}$$
$$g_1 = g + h_m/\mu_r \tag{32}$$

The radial magnetic flux density with the slot effect can be calculated from:

$$B_r(\theta_s, r) = B_g \lambda'(\theta_s, r) \tag{33}$$

where B_g is the flux density in the smooth air-gap region.

And the tangential magnetic flux density can be obtained from [30]

$$B_{\theta_s}(\theta_s, r) = B_g \lambda_{\theta s}(\theta_s, r) \tag{34}$$

with

$$\lambda_{\theta s}(\theta_s, r) = \frac{2\frac{t_c-1}{KT_w} \sum_{n=1}^{\propto} Q_n \sin(\frac{2\pi nx}{T_w})[\cosh(\frac{\pi gn}{T_w})]^{-1}}{1 - 2\frac{t_c-1}{K\pi g} \sum_{n=1}^{\propto} \frac{(-1)^n Q_n}{n}} \tag{35}$$

$$t_c = \frac{T_w(5g + w_s)}{T_w(5g + w_s) - w_s^2} \tag{36}$$

$$K = -\sum_{n=1}^{\propto} \frac{2(-1)^n Q_n}{T_w \sinh(\frac{\pi gn}{T_w})} \tag{37}$$

$$Q_n = \int_0^{\frac{w_s}{2}} [\frac{1}{\sqrt[3]{w_s/2 - x}} - \frac{1}{\sqrt[3]{w_s/2 + x}}] \sin(\frac{2\pi nx}{T_w})dx \tag{38}$$

where, T_w is the slot width.

C. DETERMINATION OF THE BOUNDARY CONDITIONS AND THE INTEGRATION COEFFICIENT

In each subdomain region, the integration coefficients can be calculated according to the boundary conditions and interface conditions. The radial flux density B_r and the tangential field strength H_θ are adopted to define these conditions as follows:

$$r = R_b : H_{\theta 1} = 0 \quad \forall \theta_s \tag{39}$$

$$r = R_{pm} : \begin{cases} B_{r1} = B_{r2} \\ H_{\theta 1} = H_{\theta 2} \end{cases} \quad \forall \theta_s \tag{40}$$

$$r = R_g : B_{r2} = B_{r3}$$
$$\text{or} \quad A_{r2} = A_{r3} \theta_s \in (\pi - \frac{\theta_2}{2}, \pi + \frac{\theta_2}{2}) \tag{41}$$

$$r = R_g : H_{\theta 2} \begin{cases} = H_{\theta 3} & \theta_s \in (\pi - \frac{\theta_2}{2}, \pi + \frac{\theta_2}{2}) \\ 0 & otherwise \end{cases} \tag{42}$$

$$r = R_s : B_{r4} = B_{r3} \theta_s \in (\pi - \frac{\theta_2}{2}, \pi + \frac{\theta_2}{2})$$
$$\text{or} \quad A_{r4} = A_{r3} \tag{43}$$

$$r = R_s : H_{\theta 4} \begin{cases} = H_{\theta 3} & \theta_s \in (\pi - \frac{\theta_2}{2}, \pi + \frac{\theta_2}{2}) \\ 0 & otherwise \end{cases} \tag{44}$$

By applying the above boundary conditions and interface conditions, the unknown integration coefficients $A_{1n} \sim D_{4n}$ can be obtained, and the derivation process is given in the Appendix.

IV. FORCE CALCULATION AND BACK-EMF PREDICT OF THE T-LPMOG

According to the foregoing analytical field model, the electromagnetic performance of the T-LPMOG can be calculated, and the force is obtained from the air-gap flux density based on the Maxwell stress tensor [41]:

$$F_d = \frac{Lr^2}{\mu_0} \int_0^{2\pi} B_{r2} B_{\theta 2} d\theta \tag{45}$$

where, F_d, F_r and F_θ represent the detent force, approximate normal force, and thrust force, respectively. L is the axial length, and r is the radii of the air-gap surface.

According to Faraday's law, the magnitude of the back-EMF can be calculated as follows:

$$E_a = -V \sum_{i=1}^{N} \frac{N_s d\phi_i}{dr} = -V \sum_{i=1}^{N} N_s \int_{\theta_i}^{\theta_i + \theta_y} B_g \lambda'(\theta_s, r) d\theta \tag{46}$$

where N is the number of coils in a series of one phase. N_s is the number of coils, V represents the speed of oscillation, θ_i is the mechanical position of the *ith* coil, and θ_y is the coil pitch.

TABLE 1. Parameters of the T-LPMOG.

Symbol	Quantity	Value
L_s	Axial length of primary	264 mm
r_g	Radius of air-gap	165.5 mm
h_s	Height of stator	34 mm
g	Length of air-gap	1 mm
h_m	Thickness of permanent magnet	5 mm
L_m	Length of permanent magnet	19 mm
w_s	Slot width	10 mm
a_p	Pole pitch	24 mm
μ_r	Relative permeability	1.09 T
B_r	Remanence of PM	1.27 T

V. VALIDATION OF THE ANALYTICAL METHOD BY THE FEM AND EXPERIMENTS

To confirm and assess the merits of the proposed analytical model, the FEA method and experimental tests are adopted to investigate the distribution of the magnetic field and the back-EMF of the T-LPMOG. The main parameters of this prototype machine used for validation are presented in Table 1, and the corresponding transformed parameters are presented in Table 2. In the FEA method, the material used for the primary iron and the secondary back iron is steel_1010.

The two different positions of the flux-line distribution in the 2-D FE model are shown in Fig. 4, and the magnetic flux density distribution in the middle position without a slot effect are given in Fig. 5.

TABLE 2. Corresponding transformed parameters of the T-LPMOG.

Symbol	Quantity	Value
L_{ex}	Extended length of secondary	2000 mm
R_s	Outer radius of stator	353.3 mm
R_g	Inner radius of stator	319.3 mm
R_{pm}	Outer radius of PM	318.3 mm
R_b	Outer radius of back-iron	313.3 mm
θ_3	Span angle of end-region	312.48 deg
θ_m	Span angle of PM	3.42 deg
θ_p	Span angle of pole pitch	4.32 deg

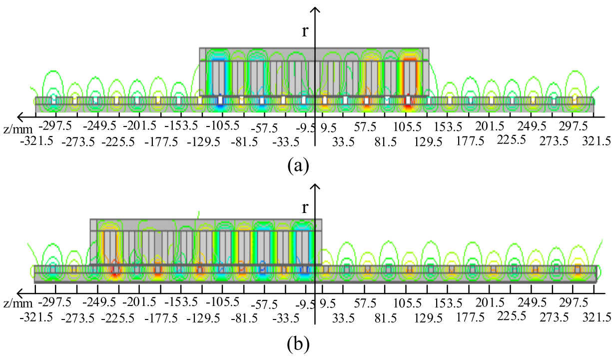

FIGURE 4. Different positions of the flux-line distribution in the T-LPMOG. a. Oscillation of the middle position of the machine. b. Oscillation of the end position of the machine.

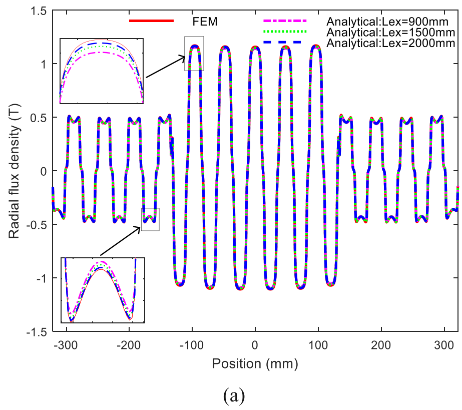

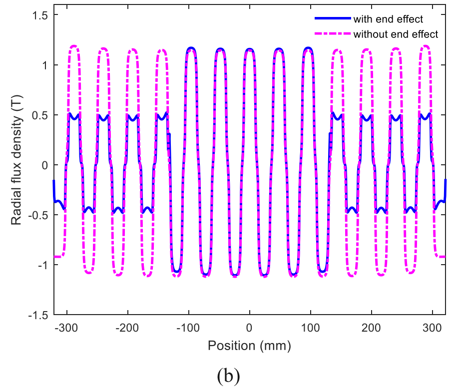

FIGURE 5. Flux density distribution of the air gap in the T-LPMOG. a. Radial flux density distribution in the slotless machine. b. Comparison of the radial flux density with and without the end effect.

Fig. 5 shows the air-gap magnetic flux density distribution without considering the slot effect. Three different radii of L_{ex} are compared in Fig. 5(a). Fig. 5(a) shows that with the increase in L_{ex}, the analytical solutions are in good agreement with the FEA results. The accuracy of the analysis model is related to the radius L_{ex}. With the increase in radius, the coincidence degree of the analytical model increases. The following shows the magnetic density distribution of the air gap with the slotted effect when L_{ex} is 2000 mm.

Fig. 5(b) compares the radial magnetic flux density distribution in the end region. From Fig. 5(b), it can be found that if the end effect is considered, then the peak value of the air-gap flux density in end regions is approximately 0.5 T. However, without considering the end effect, the flux density in the end regions is basically the same as that in the iron regions, and the error is approximately 57%, leading to an inaccurate magnetic field distribution and affecting the distribution of the detent force. Therefore, according to the comparison, the proposed 2-D analytical model can accurately predict the magnetic flux density of the end region.

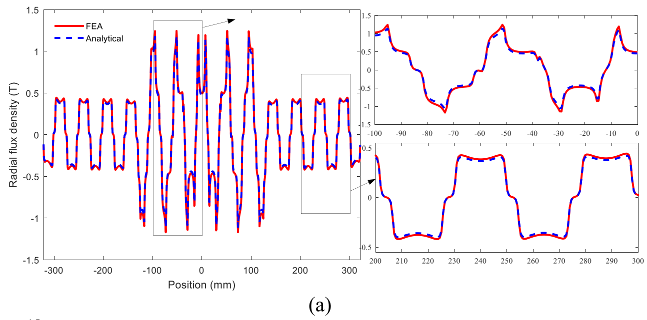

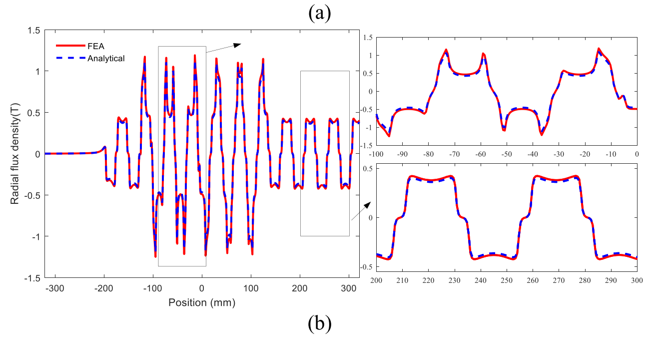

FIGURE 6. Air-gap flux density distribution between the analytical result and the FEA method. a. Oscillation of the middle position of the machine. b. Oscillation of the end position of the machine.

The air-gap flux density distributions of the T-LPMOG when the stator is located at different positions, as determined by the analytical results and the FEM simulations, are compared in Fig. 6 and Fig. 7. In the air-gap region, the influence of the flux density in each radial position is different because different positions have different relative permeances. Fig. 6 indicates that the positions between -132 mm and 132 mm are in the stator region, and the flux density obtained by the analytical method and the FEA are approximately 1.17 T and 1.24 T, respectively. The remaining parts are end regions, with a flux density of 0.45 T. Similarly, Fig. 7 shows the tangential flux density distribution of the air gap in the different oscillation positions.

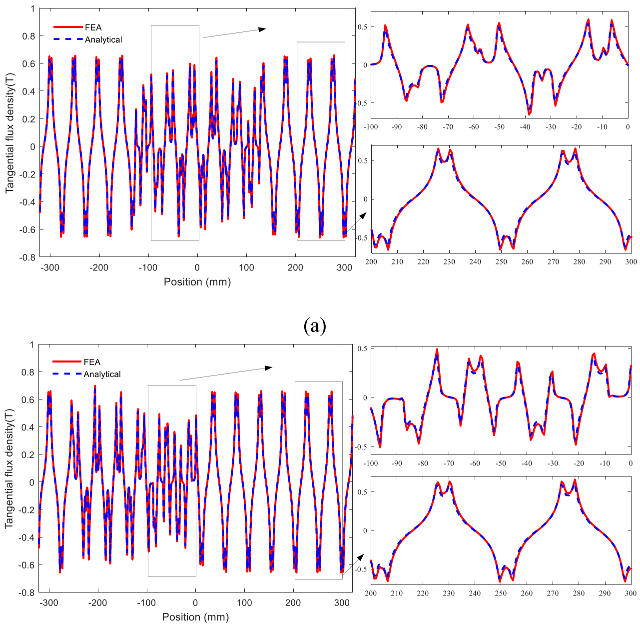

(a)

(b)

FIGURE 7. Tangential flux density distribution of the air gap between the analytical result and the FEA. a. Oscillation of the middle position of the machine. b. Oscillation of the end position of the machine.

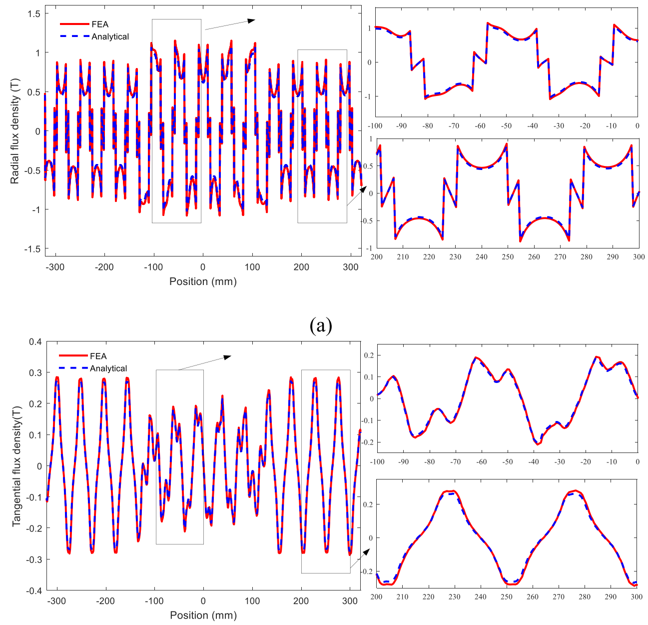

(a)

(b)

FIGURE 8. Flux density distribution of the PM region between the analytical result and the FEA at the middle position of oscillation. a. Radial flux density distribution of the middle position of the machine. b. Tangential flux density distribution of the end position of the machine.

As shown in Fig. 6 and Fig. 7, the air-gap flux density distribution of the analytical results is in good agreement with the FEM simulations. Fig. 8 compares the flux density distributions of the PM region results between the analytical and FEM solutions when the stator is in the balance position of the oscillation. In the PM region, because of the slot effect, the magnetic flux distribution of the permanent magnets under the stator teeth is different from that of the end-region distribution. The permanent magnetic flux density in the slot section is approximately 1.13 T, and that at the end region is approximately 0.85 T. As shown in Fig. 8, the flux density distribution of the PM determined by the analytical method matches well with the result using the FEA. The small difference between FEA and the analytical solutions may be caused by the magnetic nonlinearity of the iron cores, and the analytical solution depends on the length L_{ex}. A large value of L_{ex} corresponds to a highly accurate solution.

Fig. 9 shows a comparison of the detent force based on the FEA and analytical solutions. From Fig. 9, the detent force obtained by the analytical method and the FEA are approximately 42 N and 45 N, respectively, and the maximum error is approximately 5%. One explanation is that to reduce the computation time, higher harmonics are ignored in the analytical model, and if the higher harmonics are considered, length Lex of the analytical model should be sufficiently long to avoid this effect. The other explanation is that the discretization effects of the FEA and the force calculation are sensitive to the mesh quality in the air gap, and the analytical model cannot accurately consider this factor. From Fig. 9,

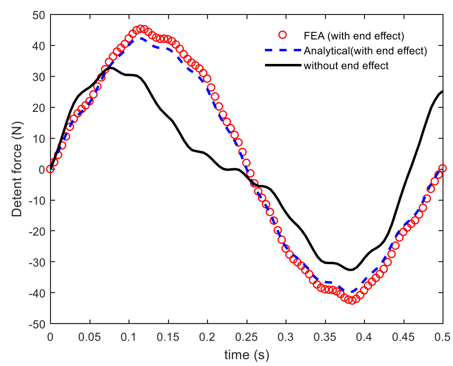

FIGURE 9. Detent force distribution of the T-LPMOG between the analytical result and the FEA method.

if we do not consider the end effect, then the detent force is approximately 30 N, which is 33% smaller than the actual value.

The single phase back-EMF distributions obtained from the analytical and FEA simulation results are compared in Fig. 10.

The back-EMF distributions of the T-LPMOG are compared in Fig. 10. Fig. 10 shows that the amplitude and frequency of the output voltage of the T-LPMOG change continually over time because when the mover moves to the balance position, the speed of the mover reaches its maximum; the movement speed is then constantly reduced, causing the value to become 0 until the mover reaches the end of the machine. A comparison of these results indicates that the

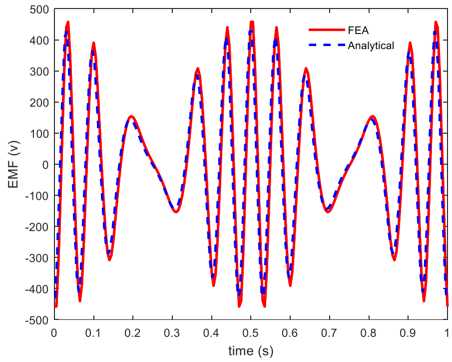

FIGURE 10. Back-EMF distribution of the one-phase obtained using the analytical and FEA methods under the no-load condition.

analytical results match the FEA results well: the maximum value of the analytically obtained three-phase back-EMF is approximately 425 V, and the value obtained using FEA is approximately 457 V. The difference between the analytical and FEA solution is that the Back-EMF calculation is related to the accuracy of the magnetic field solutions. The curvature of analytical model should be small enough to avoid the higher harmonic to improve the accuracy of the magnetic field analysis results.

The manufactured prototype machine is shown in Fig. 11. The conventional rotary motor is used in the drive motor, and the structure of the cylinder type linear motor is adopted in the linear motor. The working principle of this device is as follows: first, the belt is used to drive the flywheel; next, the flywheel drives the linear motor up and down by means of a crank-connected rod device; finally, electrical energy is produced by the relative motion between the mover and the stator.

As shown in Fig. 11(b), when the mover of the T-LPMOG moves to the vicinity of the balance position, a large-amplitude and high-frequency signal is induced in the stator coil. When the mover of the T-LPMOG moves to the upper or lower end position, the relative velocity between the stator and the mover is small, inducing a small output voltage at a low frequency in the stator coil. The test waveform in Fig. 11(e) indicates that the maximum value of the analytical three-phase back-EMF in the experiment is approximately 440 V. Fig. 11(f) and Fig. 11(e) show a comparison of the back-EMF obtained using the analytical model for the FEA results and experimental measurements. Few differences were observed between them for two reasons. 1) Fourier transform is defined for a finite length sequence, and it needs to be intercepted in the time domain, causing truncation error. 2) A barrier effect in the Fourier transform results in some discrepancy in the calculated frequency, amplitude, and phase of the result.

In addition, comparison of the computer time between the FEM and analytical model, CPU-3.6 GHz, and RAM 32.0GB desktop PC are employed in the simulation, with 120 min spent in the no-load condition, while the proposed analytical

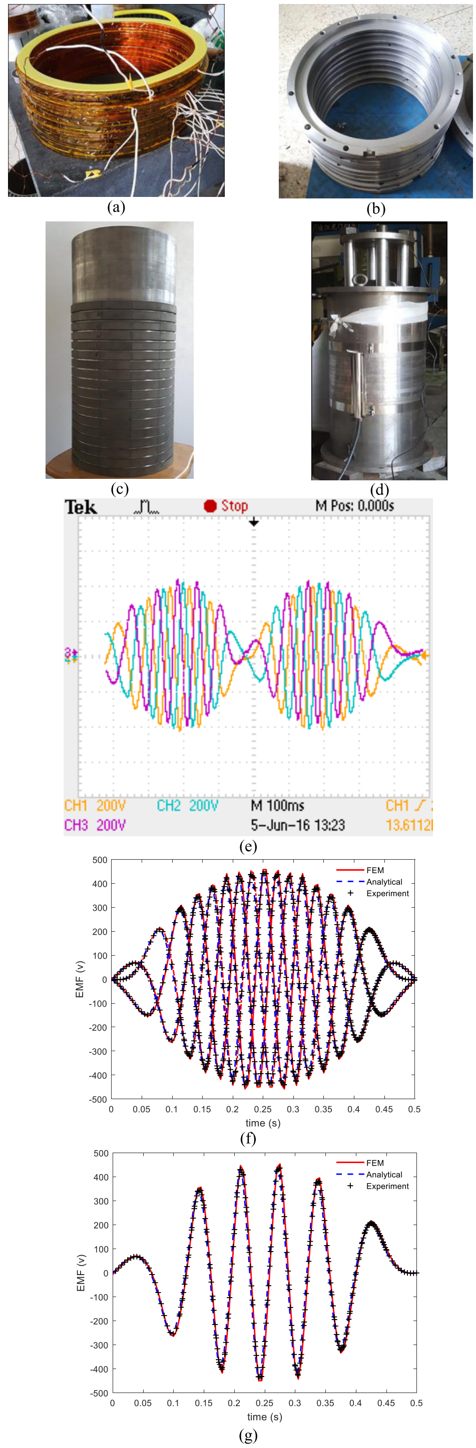

FIGURE 11. Prototype and test waveform under the no-load condition of the T-LPMOG. a. Winding of the T-LPMOG. b. Stator of the T-LPMOG. c. PM mover of the T-LPMOG. d. Prototype of the T-LPMOG. e. Test waveform of the T-LPMOG under the no-load condition. f. Distribution of the three phases of the back-EMF obtained using the analytical, FEA, and experimental methods. g. Distribution of the one-phase back-EMF obtained using the analytical, FEA, and experimental methods.

model is nearly less than 25 s. Therefore, the proposed subdomain analytical model can provide an effective technique for the initial design of the linear machine.

VI. CONCLUSION

We have presented a simplified 2-D analytical subdomain model for the design and analysis of a tubular T-LPMOG. The end effect and the slot effect were both considered. A coordinate transformation method was adopted to establish a 2-D subdomain analytical model, the cylindrical coordinates were converted to polar coordinates, and the T-LPMOG was analysed using this polar coordinate system. Based on the simplified 2-D analytical model, the flux density and back-EMF were obtained. The analytical results were verified using FEA. The results showed that the analytical results are in good agreement with the FEM simulations. The maximum error was approximately 7%, which could have been caused by the nonlinearity magnetic effect and the equivalent length of the analytical model. Moreover, a prototype of the T-LPMOG was manufactured and tested, and the experimental results were found to match well with the calculated results. Thus, the proposed analytical model could be used in the initial design and optimization of the T-LPMOG.

APPENDIX

A. INTERFACE BETWEEN THE PM REGION AND THE AIR-GAP REGION

According to equations (8), (11), (17), and (40), the following coefficient equations can be deduced:

$$A_{1n}(1+E_{1n}^2) - A_{2n}E_{2n} - B_{2n} = -F_{2n(R_{pm})}M_{\theta cn} + F_{3n(R_{pm})}M_{rsn} \quad (47)$$

$$C_{1n}(1+E_{1n}^2) - C_{2n}E_{2n} - D_{2n} = -F_{2n(R_{pm})}M_{\theta sn} - F_{3n(R_{pm})}M_{rcn} \quad (48)$$

$$A_{1n}(1-E_{1n}^2) - \mu_r A_{2n}E_{2n} + \mu_r B_{2n} = R_{pm}[S_{1sn(R_{pm})}M_{rsn} - \mu_0(1+S_{1cn(R_{pm})}M_{\theta cn})]/n \quad (49)$$

$$C_{1n}(1-E_{1n}^2) - \mu_r C_{2n}E_{2n} + \mu_r D_{2n} = -R_{pm}[S_{1cn(R_{pm})}M_{\theta sn} + \mu_0(1+S_{1sn(R_{pm})}M_{rcn})]/n \quad (50)$$

with

$$S_{1cn(r=R_{pm})} = \begin{cases} \frac{1}{n^2-1}(1-n^2(\frac{R_b}{R_{pm}})^{n+1}) & (n \neq 1) \\ \frac{1}{2}[-(1-InR_b)(\frac{R_b}{R_{pm}})^2 - Inr - 1] & (n = 1) \end{cases} \quad (51)$$

$$S_{1sn(r=R_{pm})} = \begin{cases} \frac{1}{n^2-1}(n-n^2(\frac{R_b}{R_{pm}})^{n+1}) & (n \neq 1) \\ -\frac{1}{2}[-(1+InR_b)(\frac{R_b}{R_{pm}})^2 + Inr + 1] & (n = 1) \end{cases} \quad (52)$$

Equations (47)–(50) can be rewritten in matrix format as follows:

$$K_{11}A_{1n} - K_{12}A_{2n} - K_{13}B_{2n} = Y_1 \quad (53)$$
$$K_{11}C_{1n} - K_{12}C_{2n} - K_{13}D_{2n} = Y_2 \quad (54)$$
$$K_{11}C_{1n} - K_{12}C_{2n} - K_{13}D_{2n} = Y_2 \quad (55)$$
$$K_{21}C_{1n} - K_{22}C_{2n} - K_{23}D_{2n} = Y_4 \quad (56)$$

with

$$K_{11} = I_N + E_1^2 \quad (57)$$
$$K_{12} = diag((R_{pm}/R_g)^1 \cdots (R_{pm}/R_g)^n) \quad (58)$$
$$K_{13} = I_N \quad (59)$$
$$K_{21} = I_N - E_1^2 \quad (60)$$
$$K_{22} = diag(\mu_r(R_{pm}/R_g)^1 \cdots \mu_r(R_{pm}/R_g)^n) \quad (61)$$
$$K_{23} = \mu_r I_N \quad (62)$$
$$Y_1 = F_{3(r=R_{pm})}M_{rsn} - F_{2(r=R_{pm})}M_{\theta cn} \quad (63)$$
$$Y_2 = -F_{2(r=R_{pm})}M_{\theta sn} - F_{3(r=R_{pm})}M_{rcn} \quad (64)$$
$$Y_3 = R_{pm}/n[S_{1sn(r=R_{pm})}M_{rsn} - \mu_0(1+S_{1cn(r=R_{pm})}M_{\theta cn})] \quad (65)$$
$$Y_4 = -R_{pm}/n[S_{1cn(r=R_{pm})}M_{\theta sn} + \mu_0(1+S_{1sn(r=R_{pm})}M_{rcn})] \quad (66)$$

B. INTERFACE BETWEEN THE AIR GAP AND END REGION

The boundary condition between the air-gap region and the end region or air-gap region and slot region are defined as follows:

$$r = R_g : H_{\theta 2} \begin{cases} = H_{\theta 3} & \theta_s \in (\pi - \frac{\theta_2}{2}, \pi + \frac{\theta_2}{2}) \\ 0 & otherwise \end{cases}$$

The tangential field strength in the end region and slot region can be obtained from the vector potential as follows:

$$H_{3\theta} = \frac{1}{\mu_0}\sum_{k=1}^{\propto}[A_{3k}P_{3k(R_g)} + B_{3k}J_{3k(R_g)}] \times \cos(\frac{k\pi}{\theta_3}(\theta_s + \frac{\theta_3}{2} - \pi)) \quad (67)$$

$$P_{3k(R_g)} = -\frac{k\pi}{\theta_3}\frac{1}{R_s}(\frac{r}{R_s})^{\frac{k\pi}{\theta_3}-1} \quad (68)$$

$$J_{3k(R_g)} = \frac{k\pi}{\theta_3}\frac{1}{R_g}(\frac{r}{R_g})^{-\frac{k\pi}{\theta_3}-1} \quad (69)$$

The tangential field strength in the end region must be expanded using a Fourier series:

$$H_{3\theta}^s = \sum_{n=1}^{\propto} A_{sn}\cos(n\theta_s) + B_{sn}\sin(n\theta_s) \quad (70)$$

According to equations (8), (21), and (42), the following coefficient equations can be deduced:

$$-A_2\frac{1}{\mu_0}\frac{n}{R_g} + B_2\frac{1}{\mu_0}\frac{n}{R_g}(\frac{R_{pm}}{R_g})^n = [A_3H_{3k(r=R_g)} + B_3J_{3k(r=R_g)}]\eta_{(kn)} \quad (71)$$

$$-C_2\frac{1}{\mu_0}\frac{n}{R_g} + D_2\frac{1}{\mu_0}\frac{n}{R_g}(\frac{R_{pm}}{R_g})^n = [A_3H_{3k(r=R_g)} + B_3J_{3k(r=R_g)}]\varsigma_{(kn)} \quad (72)$$

where

$$\eta_{(kn)} = \begin{cases} -\frac{1}{\pi}\frac{n\theta_3}{(k\pi)^2-(n\pi)^2} \times [\cos(k\pi)\sin n(\frac{\theta_3}{2}+\pi) \\ -\sin(n(\pi-\frac{\theta_3}{2}))] \quad n\theta_3 \neq k\pi \\ \frac{1}{\pi}\frac{\theta_3}{2}\cos(\frac{k\pi}{\theta_3}(\frac{\theta_3}{2}-\pi))+\frac{1}{4n\pi} \\ \times[\cos(k\pi)\sin n(\frac{\theta_3}{2}+\pi)-\sin(n(\pi-\frac{\theta_3}{2})] \\ \qquad n\theta_3 = k\pi \end{cases} \tag{73}$$

$$\varsigma_{(kn)} = \begin{cases} -\frac{1}{\pi}\frac{n\theta_3}{(k\pi)^2-(n\pi)^2} \times [\cos(k\pi)\cos n(\frac{\theta_3}{2}+\pi) \\ -\cos(n(\pi-\frac{\theta_3}{2}))] \quad n\theta_3 \neq k\pi \\ \frac{1}{\pi}\frac{\theta_3}{2}\sin(\frac{k\pi}{\theta_3}(\frac{\theta_3}{2}-\pi))-\frac{1}{4n\pi} \\ \times[\cos(k\pi)\cos n(\frac{\theta_3}{2}+\pi)-\cos(n(\pi-\frac{\theta_3}{2})] \\ \qquad n\theta_3 = k\pi \end{cases} \tag{74}$$

Equations (71) and (72) can be rewritten in matrix format as follows:

$$-K_{32}A_2 + K_{33}B_2 - K_{37}A_3 - K_{38}B_3 = 0 \tag{75}$$

$$-K_{32}C_2 + K_{33}D_2 - K_{67}A_3 - K_{68}B_3 = 0 \tag{76}$$

The magnetic vector potential in the air-gap region must be expanded using Fourier series:

$$A_{z2}^{3s} = \sum_{k=1}^{\propto} Q_{2k}^3 \cos\frac{k\pi}{\theta_3}(\theta_s+\frac{\theta_3}{2}-\pi) \quad \theta_s \in (\pi-\frac{\theta_3}{2}, \pi+\frac{\theta_3}{2}) \tag{77}$$

where

$$Q_{2k}^3 = \sum_{n=1}^{\propto}[A_{2n}(\frac{r}{R_g})^n + B_{2n}(\frac{r}{R_{pm}})^{-n}]\frac{2\pi}{\theta_3}\eta_{(kn)} + \sum_{n=1}^{\propto}[C_{2n}(\frac{r}{R_g})^n + D_{2n}(\frac{r}{R_{pm}})^{-n}]\frac{2\pi}{\theta_3}\zeta_{(kn)} \tag{78}$$

According to equations (22), (77), and (41), the following coefficient equations can be obtained:

$$A_{3k}G_{31k} + B_{3k}G_{32k} = Q_{2k}^3 \tag{79}$$

Equation (79) can be rewritten in matrix format as follows:

$$K_{77}A_3 + K_{78}B_3 - K_{72}A_2 - K_{73}B_2 - K_{75}C_2 - K_{76}D_2 = 0 \tag{80}$$

with

$$K_{77} = diag(G_{31k}) \tag{81}$$

$$K_{78} = diag(G_{32k}) \tag{82}$$

$$K_{72} = 2\pi/\theta_3\eta_{(kn)}I_{kn} \tag{83}$$

$$K_{73} = 2\pi/\theta_3 \times \zeta_{(kn)} \times diag((\frac{r}{R_{pm}})^{-1}\dots(\frac{r}{R_{pm}})^{-n}) \tag{84}$$

$$K_{75} = 2\pi/\theta_3 \times \zeta_{(kn)}I_{kn} \tag{85}$$

$$K_{76} = 2\pi/\theta_3 \times \zeta_{(kn)} \times diag((\frac{r}{R_{pm}})^{-1}\dots(\frac{r}{R_{pm}})^{-n}) \tag{86}$$

C. INTERFACE BETWEEN THE END REGION AND THE EXTERIOR REGION

According to equations (8), (11), (70), and (44), the following coefficient equations can be obtained:

$$B_4\frac{n}{R_s}\frac{1}{\mu_0} = \sum_{k=1}^{\propto}[A_3P_{3k(r=R_g)} + B_3J_{3k(r=R_g)}]\eta_{(kn)} \tag{87}$$

$$D_4\frac{n}{R_s}\frac{1}{\mu_0} = \sum_{k=1}^{\propto}[A_3P_{3k(r=R_g)} + B_3J_{3k(r=R_g)}]\varsigma_{(kn)} \tag{88}$$

Thus, equations (87) and (88) can be rewritten in matrix format as follows:

$$K_{97}A_3 + K_{98}B_3 - K_{99}B_4 = 0 \tag{89}$$

$$K_{07}A_3 + K_{08}B_3 - K_{99}D_4 = 0 \tag{90}$$

with

$$K_{97} = \eta'_{(kn)} \times diag(P_{31(r)}\cdots P_{3k(r)}) \tag{91}$$

$$K_{98} = \eta'_{(kn)} \times diag(J_{31(r)}\cdots J_{3k(r)}) \tag{92}$$

$$K_{99} = diag(1/\mu_0R_s\cdots n/\mu_0R_s) \tag{93}$$

$$K_{07} = \varsigma'_{(kn)} \times diag(P_{31(r)}\cdots P_{3k(r)}) \tag{94}$$

$$K_{08} = \varsigma'_{(kn)} \times diag(J_{31(r)}\cdots J_{3k(r)}) \tag{95}$$

$$\begin{bmatrix} K_{11} & -K_{12} & -K_{13} & 0 & 0 & 0 & 0 & 0 & 0 & 0 \\ 0 & 0 & 0 & K_{11} & -K_{12} & -K_{13} & 0 & 0 & 0 & 0 \\ K_{21} & -K_{22} & -K_{23} & 0 & 0 & 0 & 0 & 0 & 0 & 0 \\ 0 & 0 & 0 & K_{21} & -K_{22} & -K_{23} & 0 & 0 & 0 & 0 \\ 0 & -K_{32} & K_{33} & 0 & 0 & 0 & -K_{37} & -K_{38} & 0 & 0 \\ 0 & 0 & 0 & 0 & -K_{32} & K_{33} & -K_{67} & -K_{68} & 0 & 0 \\ 0 & -K_{72} & -K_{73} & 0 & -K_{75} & -K_{76} & K_{77} & K_{78} & 0 & 0 \\ 0 & 0 & 0 & 0 & 0 & 0 & K_{97} & K_{98} & -K_{99} & 0 \\ 0 & 0 & 0 & 0 & 0 & 0 & K_{07} & K_{08} & 0 & -K_{99} \\ 0 & 0 & 0 & 0 & 0 & 0 & K_{87} & K_{88} & -K_{89} & -K_{80} \end{bmatrix} \begin{bmatrix} A_1 \\ A_2 \\ B_2 \\ C_1 \\ C_2 \\ D_2 \\ A_3 \\ B_3 \\ B_4 \\ D_4 \end{bmatrix} = \begin{bmatrix} Y_1 \\ Y_2 \\ Y_3 \\ Y_4 \\ 0 \\ 0 \\ 0 \\ 0 \\ 0 \\ 0 \end{bmatrix} \tag{104}$$

The magnetic vector potential in the exterior region must be expanded using a Fourier series:

$$A^s_{4r} = \sum_{k=1}^{\propto} P_{2k} \cos \frac{k\pi}{\theta_3}(\theta_s + \frac{\theta_3}{2} - \pi) \quad \theta_s \in (\pi - \frac{\theta_3}{2}, \pi + \frac{\theta_3}{2}) \tag{96}$$

where

$$P_{2k} = \sum_{n=1}^{\propto} B_4(\frac{r}{R_{pm}})^{-n} \frac{2\pi}{\theta_3} \eta_{(kn)} + \sum_{n=1}^{\propto} D_4(\frac{r}{R_{pm}})^{-n} \frac{2\pi}{\theta_3} \varsigma_{(kn)} \tag{97}$$

According to equations (22), (43), (44), and (96), the following coefficient equations can be obtained:

$$A_3 G_1 + B_3 G_2 = P_{2k} \tag{98}$$

Equation (98) can be rewritten in matrix form as follows:

$$K_{87} A_3 + K_{88} B_3 - K_{89} B_4 - K_{80} D_4 = 0 \tag{99}$$

with

$$K_{87} = I_N \tag{100}$$

$$K_{88} = diag(G_2) \tag{101}$$

$$K_{89} = 2\pi/\theta_3 \eta_{(kn)} I_N \tag{102}$$

$$K_{80} = 2\pi/\theta_3 \varsigma_{(kn)} I_N \tag{103}$$

Finally, the above coefficient equations can be rewritten as matrix equation (104), as shown at the bottom of the previous page. By solving this matrix, the unknown coefficients can be derived; according to these coefficients, the magnetic field distribution can be analysed.

REFERENCES

[1] *IEEE Draft Standard Criteria for Diesel-Generator Units Applied as Standby Power Supplies for Nuclear Power Generating Stations*, IEEE Standard P387DD2017, Jan. 2017, pp. 1–54.

[2] M. Johnson, M. C. Gardner, and H. A. Toliyat, "Design and analysis of an axial flux magnetically geared generator," *IEEE Trans. Ind. Appl.*, vol. 53, no. 1, pp. 97–105, Jan./Feb. 2017.

[3] A. M. El-Refaie, M. R. Shah, and K.-K. Huh, "High-power-density fault-tolerant PM generator for safety-critical applications," *IEEE Trans. Ind. Appl.*, vol. 50, no. 3, pp. 1717–1728, May/Jun. 2014.

[4] T. Xia, H. Yu, Z. Chen, L. Huang, X. Liu, and M. Hu, "Design and analysis of a field-modulated tubular linear permanent magnet generator for direct-drive wave energy conversion," *IEEE Trans. Magn.*, vol. 53, no. 6, pp. 1–4, Jun. 2017.

[5] C. Liu, H. Yu, M. Hu, Q. Liu, and S. Zhou, "Detent force reduction in permanent magnet tubular linear generator for direct-driver wave energy conversion," *IEEE Trans. Magn.*, vol. 49, no. 5, pp. 1913–1916, May 2013.

[6] C. Liu, H. Yu, M. Hu, Q. Liu, S. Zhou, and L. Huang, "Research on a permanent magnet tubular linear generator for direct drive wave energy conversion," *IET Renew. Power Gener.*, vol. 8, no. 3, pp. 281–288, Apr. 2014.

[7] L. Xu, M. Lin, and X. Fu, "End-effects analysis and experimental study of a double stator linear-rotary permanent magnet motor with long mover," *IET Electr. Power Appl.*, vol. 11, no. 9, pp. 1601–1609, 2017.

[8] M. N. Ma and L. Y. Li, "Modeling and flux leakage analysis for long-stator PM linear motor including longitudinal end effects," in *Proc. IEEE Int. Conf. Appl. Supercond. Electromagn. Devices (ASEMD)*, Nov. 2015, pp. 494–495.

[9] A. L. Li, B. M. Ma, and C. Q. Chen, "Detent force analysis in permanent magnet linear synchronous motor considering longitudinal end effects," in *Proc. 15th Int. Conf. Elect. Mach. Syst. (ICEMS)*, 2012, pp. 1–5.

[10] Y.-M. Chen, S.-Y. Fan, and W.-S. Lu, "Performance analysis of linear permanent-magnet motors with finite-element analysis," *IEEE Trans. Magn.*, vol. 44, no. 3, pp. 377–385, Mar. 2008.

[11] B. Tomczuk, G. Schroder, and A. Waindok, "Finite-element analysis of the magnetic field and electromechanical parameters calculation for a slotted permanent-magnet tubular linear motor," *IEEE Trans. Magn.*, vol. 43, no. 7, pp. 3229–3236, Jul. 2007.

[12] J. Chang, D. H. Kang, I.-A. Viorel, and S. Larisa, "Transverse flux reluctance linear motor's analytical model based on finite-element method analysis results," *IEEE Trans. Magn.*, vol. 43, no. 4, pp. 1201–1204, Apr. 2007.

[13] T. Yamaguchi, Y. Kawase, M. Yoshida, Y. Saito, and Y. Ohdachi, "3-D finite element analysis of a linear induction motor," *IEEE Trans. Magn.*, vol. 37, no. 5, pp. 3668–3671, Sep. 2001.

[14] J. Y. Song, J. H. Lee, D. W. Kim, Y. J. Kim, and S. Y. Jung, "Analysis and modeling of concentrated winding variable flux memory motor using magnetic equivalent circuit method," *IEEE Trans. Magn.*, vol. 53, no. 6, pp. 1–4, Jun. 2017.

[15] J.-K. Park, T. R. Wellawatta, Z. Ullah, and J. Hur, "New equivalent circuit of the IPM-type BLDC motor for calculation of shaft voltage by considering electric and magnetic fields," *IEEE Trans. Ind. Appl.*, vol. 52, no. 5, pp. 3763–3771, Sep./Oct. 2016.

[16] K.-D. Lee, J. Lee, and H.-W. Lee, "Inductance calculation of flux concentrating permanent magnet motor through nonlinear magnetic equivalent circuit," *IEEE Trans. Magn.*, vol. 51, no. 11, Nov. 2015, Art. no. 8204304.

[17] H.-K. Yeo, D.-K. Lim, D.-K. Woo, J.-S. Ro, and H.-K. Jung, "Magnetic equivalent circuit model considering overhang structure of a surface-mounted permanent-magnet motor," *IEEE Trans. Magn.*, vol. 51, no. 3, pp. 1–4, Mar. 2015.

[18] B. Sheikh-Ghalavand, S. Vaez-Zadeh, and A. H. Isfahani, "An improved magnetic equivalent circuit model for iron-core linear permanent-magnet synchronous motors," *IEEE Trans. Magn.*, vol. 46, no. 1, pp. 112–120, Jan. 2010.

[19] Z. Q. Zhu, D. Howe, E. Bolte, and B. Ackermann, "Instantaneous magnetic field distribution in brushless permanent magnet DC motors. I. Open-circuit field," *IEEE Trans. Magn.*, vol. 29, no. 1, pp. 124–135, Jan. 1993.

[20] Z. Q. Zhu and D. Howe, "Instantaneous magnetic field distribution in brushless permanent magnet DC motors. II. Armature-reaction field," *IEEE Trans. Magn.*, vol. 29, no. 1, pp. 136–142, Jan. 1993.

[21] U. Kim and D. K. Lieu, "Magnetic field calculation in permanent magnet motors with rotor eccentricity: Without slotting effect," *IEEE Trans. Magn.*, vol. 34, no. 4, pp. 2243–2252, Jul. 1998.

[22] N. Bianchi, "Analytical field computation of a tubular permanent-magnet linear motor," *IEEE Trans. Magn.*, vol. 36, no. 5, pp. 3798–3801, Sep. 2000.

[23] B. L. J. Gysen, E. A. Lomonova, J. J. H. Paulides, and A. J. A. Vandenput, "Analytical and numerical techniques for solving Laplace and Poisson equations in a tubular permanent-magnet actuator: Part I. Semi-analytical framework," *IEEE Trans. Magn.*, vol. 44, no. 7, pp. 1751–1760, Jul. 2008.

[24] B. L. J. Gysen, E. A. Lomonova, J. J. H. Paulides, and A. J. A. Vandenput, "Analytical and numerical techniques for solving Laplace and Poisson equations in a tubular permanent magnet actuator: Part II. Schwarz–Christoffel mapping," *IEEE Trans. Magn.*, vol. 44, no. 7, pp. 1761–1767, Jul. 2008.

[25] K. Abbaszadeh and F. R. Alam, "On-load field component separation in surface-mounted permanent-magnet motors using an improved conformal mapping method," *IEEE Trans. Magn.*, vol. 52, no. 2, Feb. 2016, Art. no. 5200112.

[26] Z. Q. Zhu and D. Howe, "Instantaneous magnetic field distribution in brushless permanent magnet DC motors. III. Effect of stator slotting," *IEEE Trans. Magn.*, vol. 29, no. 1, pp. 143–151, Jan. 1993.

[27] Z. Zhu and D. Howe, "Instantaneous magnetic field distribution in permanent magnet brushless dc motors. IV. Magnetic field on load," *IEEE Trans. Magn.*, vol. 29, no. 1, pp. 152–158, Jan. 1993.

[28] IEEE Journals & Magazine. *Electromagnetic Design of a High-Speed Solid Cylindrical Permanent-Magnet Motor Equipped With Active Magnetic Bearings*. Accessed: Sep. 20, 2017. [Online]. Available: http://ieeexplore.ieee.org/document/7903698/

[29] D. Žarko, D. Ban, and T. A. Lipo, "Analytical calculation of magnetic field distribution in the slotted air gap of a surface permanent-magnet motor using complex relative air-gap permeance," *IEEE Trans. Magn.*, vol. 42, no. 7, pp. 1828–1837, Jul. 2006.

[30] A. Tessarolo and M. Olivo, "A new method for the analytical determination of the complex relative permeance function in linear electric machines with slotted air gap," in *Proc. Int. Symp. Power Electron., Elect. Drives, Automat. Motion (SPEEDAM)*, 2016, pp. 1330–1335.

[31] K. Boughrara, B. L. Chikouche, R. Ibtiouen, D. Žarko, and O. Touhami, "Analytical model of slotted air-gap surface mounted permanent-magnet synchronous motor with magnet bars magnetized in the shifting direction," *IEEE Trans. Magn.*, vol. 45, no. 2, pp. 747–758, Feb. 2009.

[32] Z. J. Liu and J. T. Li, "Analytical solution of air-gap field in permanent-magnet motors taking into account the effect of pole transition over slots," *IEEE Trans. Magn.*, vol. 43, no. 10, pp. 3872–3883, Oct. 2007.

[33] Z. J. Liu and J. T. Li, "Accurate prediction of magnetic field and magnetic forces in permanent magnet motors using an analytical solution," *IEEE Trans. Energy Convers.*, vol. 23, no. 3, pp. 717–726, Sep. 2008.

[34] F. Dubas and C. Espanet, "Analytical solution of the magnetic field in permanent-magnet motors taking into account slotting effect: No-load vector potential and flux density calculation," *IEEE Trans. Magn.*, vol. 45, no. 5, pp. 2097–2109, May 2009.

[35] Y. Amara and G. Barakat, "Analytical modeling of magnetic field in surface mounted permanent-magnet tubular linear machines," *IEEE Trans. Magn.*, vol. 46, no. 11, pp. 3870–3884, Nov. 2010.

[36] Y. Amara, G. Barakat, and P. Reghem, "Armature reaction magnetic field of tubular linear surface-inset permanent-magnet machines," *IEEE Trans. Magn.*, vol. 47, no. 4, pp. 805–811, Apr. 2011.

[37] M. M. Reza, A. K. Chauhan, S. N. Mahendra, and R. K. Srivastava, "No-load magnetic field analysis of double-sided linear tubular permanent magnet synchronous machine," in *Proc. IEEE Int. Conf. Power Electron., Drives Energy Syst. (PEDES)*, Dec. 2016, pp. 1–5.

[38] A. Souissi, I. Abdennadher, and A. Masmoudi, "Analytical prediction of the no-load operation features of tubular-linear permanent magnet synchronous machines," *IEEE Trans. Magn.*, vol. 52, no. 1, Jan. 2016, Art. no. 9500507.

[39] H. Hu, J. Zhao, X. Liu, Y. Guo, and J. Zhu, "No-load magnetic field and cogging force calculation in linear permanent-magnet synchronous machines with semiclosed slots," *IEEE Trans. Ind. Electron.*, vol. 64, no. 7, pp. 5564–5575, Jul. 2017.

[40] S. Xu and X. Liu, "Magnetic field computation for high speed surface mounted permanent magnet machine with parallelly magnetized magnet segments," in *Proc. IEEE Int. Electr. Mach. Drives Conf. (IEMDC)*, May 2017, pp. 1–8.

[41] L. J. Wu, Z. Q. Zhu, D. Staton, M. Popescu, and D. Hawkins, "An improved subdomain model for predicting magnetic field of surface-mounted permanent magnet machines accounting for tooth-tips," *IEEE Trans. Magn.*, vol. 47, no. 6, pp. 1693–1704, Jun. 2011.

[42] L. J. Wu, Z. Q. Zhu, D. Staton, M. Popescu, and D. Hawkins, "Analytical prediction of electromagnetic performance of surface-mounted PM machines based on subdomain model accounting for tooth-tips," *IET Electr. Power Appl.*, vol. 5, no. 7, pp. 597–609, Aug. 2011.

[43] L. J. Wu, Z. Q. Zhu, D. Staton, M. Popescu, and D. Hawkins, "Subdomain model for predicting armature reaction field of surface-mounted permanent-magnet machines accounting for tooth-tips," *IEEE Trans. Magn.*, vol. 47, no. 4, pp. 812–822, Apr. 2011.

RONG GUO received the B.E. degree in electrical engineering from the Heilongjiang University of Science and Technology in 2011 and the M.E. degree from the Harbin University of Science and Technology. She is currently pursuing the Ph.D. degree with Southeast University. Her research interests include design and analysis the permanent-magnet linear machines, including modeling and simulation.

HAITAO YU received the B.E. and M.E. degrees from Chongqing University, Chongqing, China, in 1986 and 1989, respectively, and the D.E. degree from the Huazhong University of Science and Technology, Wuhan, China, in 1995. He has been a Professor with the School of Electrical Engineering, Southeast University, Nanjing, China, since 2003. His current research interests include linear machine and wave energy conversion.

TAO XIA received the M.S. degree in electrical engineering from Henan Polytechnic University, Jiaozuo, China, in 2015. He is currently pursuing the Ph.D. degree in electrical engineering with Southeast University, Nanjing, China. His research interests include the design and control the permanent magnet linear machines.

ZHENCHUAN SHI received the M.S. degree in electrical engineering from Southeast University in 2013, where he is currently pursuing the Ph.D. degree. His experience includes working with the Urban and Rural Grid Automation Unit, Nanjing NARI Group Co., Ltd. Since 2010, he has been an Electrical Machine Design Engineer Assistant with the Nanjing Scifine Electrical Technology Co., Ltd.

WEIBO ZHONG received the M.S. degree in electrical engineering from Southeast University, where he is currently pursuing the Ph.D. degree with the Engineering Research Center of Motion Control of MOE. His research interests include design and analysis the permanent magnet linear generator.

XIAOMEI LIU received the M.S. degree in electrical engineering from Henan Polytechnic University, Jiaozuo, China, in 2015. She is currently pursuing the Ph.D. degree in electrical engineering with Southeast University, Nanjing, China. Her research interests include the design of the permanent magnet linear machines and their thermal management.